

LETTERS

Charon's radius and atmospheric constraints from observations of a stellar occultation

A. A. S. Gulbis¹, J. L. Elliot^{1,2,3}, M. J. Person¹, E. R. Adams¹, B. A. Babcock^{4,6}, M. Emilio⁷, J. W. Gangestad^{5,6}, S. D. Kern¹, E. A. Kramer¹, D. J. Osip⁸, J. M. Pasachoff⁵, S. P. Souza⁵ & T. Tuvikene^{6,9}

The physical characteristics of Pluto and its moon, Charon, provide insight into the evolution of the outer Solar System. Although previous measurements have constrained the masses of these bodies^{1,2}, their radii and densities have remained uncertain. The observation of a stellar occultation by Charon in 1980 established a lower limit on its radius of 600 km (ref. 3) (later refined to 601.5 km; ref. 4) and suggested a possible atmosphere⁴. Subsequent, mutual event modelling yielded a range of 600–650 km (ref. 5), corresponding to a density of $1.56 \pm 0.22 \text{ g cm}^{-3}$ (refs 2, 5). Here we report multiple-station observations of a stellar occultation by Charon. From these data, we find a mean radius of $606 \pm 8 \text{ km}$, a bulk density of $1.72 \pm 0.15 \text{ g cm}^{-3}$, and rock-mass fraction 0.63 ± 0.05 . We do not detect a significant atmosphere and place 3σ upper limits on atmospheric number densities for candidate gases. These results seem to be consistent with collisional formation for the Pluto–Charon system in which the precursor objects may have been differentiated⁶, and they leave open the possibility of atmospheric retention by the largest objects in the outer Solar System.

Observing light from a star as an object passes in front of it—a stellar occultation—produces data with the highest spatial resolution available from Earth-based observing methods. Such data are critical for determining accurate sizes and probing atmospheres of distant Solar System objects; however, observations can be difficult because of the required geographic and temporal precision. A stellar occultation by Charon has been observed only once before and resulted in a single chord³.

An occultation by Charon of the star ‘C313.2’ (originally identified as a Pluto occultation candidate star ‘P313.2’⁷; UCAC2 26257135, with R- and K-band magnitudes respectively $R = 14.8$ and $K = 12.2$) was predicted to occur on 11 July 2005 (UT) (<http://occult.mit.edu/research/occultations/Charon/C313.2.html>). We arranged to observe the event from four sites in South America using five telescopes. The telescopes were the 0.6-m at Laboratório Nacional de Astrofísica’s Observatório Pico dos Dias, Itajubá, Brazil; the 0.84-m at Observatório Cerro Armazones, Antofagasta, Chile; the 2.5-m du Pont and 6.5-m Clay at Las Campanas Observatory, La Serena, Chile; and the 8-m Gemini South on Cerro Pachón, La Serena, Chile. Data were successfully obtained at all but Pico dos Dias, where the occultation was unobservable owing to clouds. The occultation occurred four days after new moon, and image quality ranged from excellent to poor at the successful observing stations (0.5–4 arcsec). The instruments employed for the observations, excluding Gemini South, were POETS (Portable Occultation, Eclipse, and Transit Systems). Each system consisted of a high-speed Andor Ixon camera, an instrument control computer, and a GPS receiver to trigger frames and establish

accurate timing. Gemini South observations were performed using the Acquisition Camera. Observation details for each site are provided in Supplementary Information.

Charon’s aspect at the time of the occultation is shown in Fig. 1, overlaid with the paths of each observed chord. The stations were spread approximately 580 km perpendicular to Charon’s motion and spanned just under half of the shadow width, with stations on both sides of the centreline. Astrometric data were recorded at each successful site roughly an hour before and after the event, with twenty minutes of contiguous high-speed data encompassing the predicted midtimes. For reducing the data that spanned the occultation, a range of square apertures was selected, containing C313.2, Pluto and Charon. We used the astrometric frames, in which C313.2

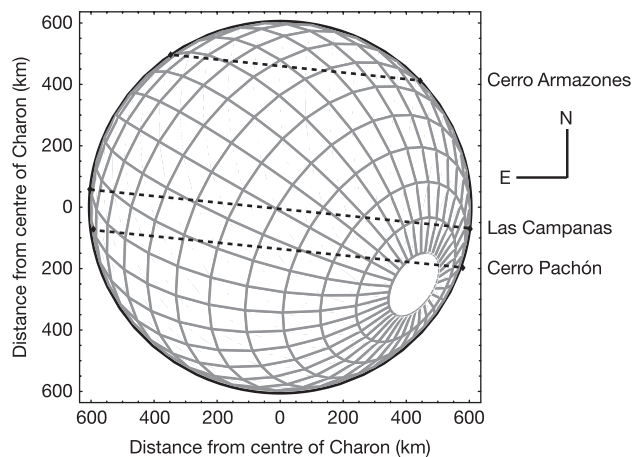


Figure 1 | Observed occultation chords. Overlaid on a diagram of Charon, dashed bold lines indicate the occultation chord paths as they appeared from each successful observing station. The coordinates (longitude, latitude) of each station are: Cerro Armazones ($70^{\circ} 11' 46'' \text{ W}$, $24^{\circ} 35' 52'' \text{ S}$), Las Campanas du Pont ($70^{\circ} 42' 13'' \text{ W}$, $29^{\circ} 00' 26'' \text{ S}$), Las Campanas Clay ($70^{\circ} 41' 33'' \text{ W}$, $29^{\circ} 00' 51'' \text{ S}$) and Cerro Pachón ($70^{\circ} 43' 24'' \text{ W}$, $30^{\circ} 13' 42'' \text{ S}$). Coordinates were obtained from POETS GPS surveys at all locations except Cerro Pachón, for which we reference the *Astronomical Almanac*²⁸. The du Pont and Clay telescopes at Las Campanas are geographically close enough that their chords are indistinguishable in this plot. Charon’s south pole (IAU coordinate convention) is visible in the lower right. The distance to Charon at the time of the occultation was 30.07 AU, and the geocentric shadow velocity was 20.93 km s^{-1} . The geometric limb times during immersion and emersion for each of these chords were used to calculate Charon’s radius.

¹Department of Earth, Atmospheric, and Planetary Sciences, ²Department of Physics, Massachusetts Institute of Technology, Cambridge, Massachusetts 02139-4307, USA.

³Lowell Observatory, Flagstaff, Arizona 86001, USA. ⁴Physics Department, ⁵Astronomy Department, Williams College, Williamstown, Massachusetts 01267-2565, USA.

⁶Instituto de Astronomía, Universidad Católica del Norte, Avda. Angamos 0610, Antofagasta, Chile. ⁷Departamento de Geociências, Universidade Estadual de Ponta Grossa, Paraná, Brazil. ⁸Las Campanas Observatory, Carnegie Observatories, Casilla 601, La Serena, Chile. ⁹Vrije Universiteit Brussel, Brussels, Belgium.

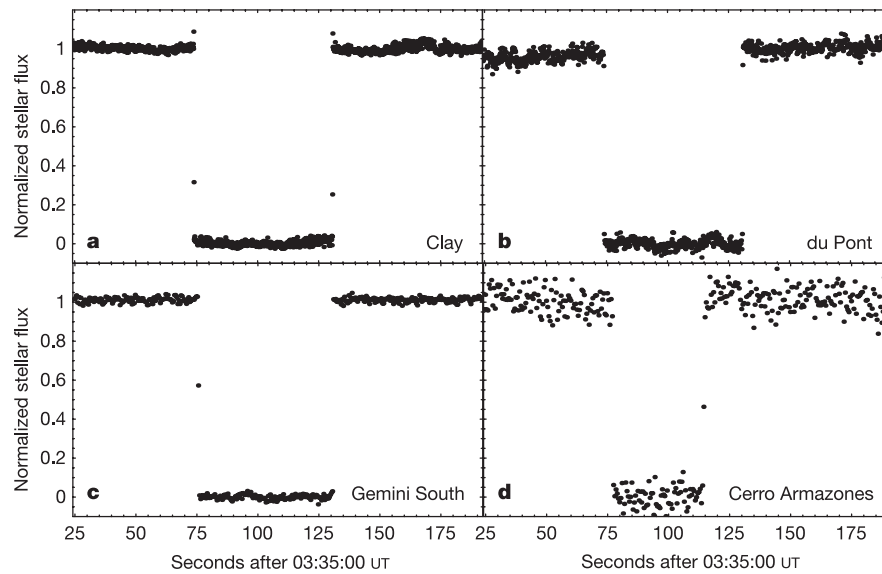


Figure 2 | Light curves showing the occultation of C313.2 by Charon. These plots display the normalized flux of the star observed at each of the four successful telescopes before, during and after the occultation. Telescopes and data rates for each of the plots are **a**, the Las Campanas 6.5-m Clay at 10 Hz, **b**, the Las Campanas 2.5-m du Pont at 5 Hz, **c**, the Cerro Pachón 8-m Gemini South at ~ 2.24 Hz, and **d**, the Cerro Armazones 0.84-m telescope at 2 Hz. Excluding Gemini South, data were obtained using POETS (frame transfer time of 1.74 ms per exposure) and no filter. Gemini South employed the Acquisition Camera and the R_G0154 filter (610–750 nm), with an integration time of 0.3 s and 0.146 ± 0.001 s required for readout. The data

remained clearly resolved from Pluto–Charon, to measure the spatial offset between a standard star and C313.2. The centre of each aperture was then set by determining the centre of the comparison star and employing the offset. The sum of the signal in the aperture, minus the background, was calculated to generate light curves. The final aperture size for each dataset was selected on the basis of highest resulting signal-to-noise ratio.

Normalized light curves from each of the sites are displayed in Fig. 2. Data from the Clay telescope had the best signal-to-noise ratio (273) and the best time resolution (0.1 s). Although Gemini South is a larger telescope, the throughput was limited by an R filter and data were taken at a significantly slower cadence (0.3 s integration time, with ~ 0.15 s deadtime). The spatial resolutions of the datasets are 2.13 km (Clay), 4.27 km (du Pont), 10.66 km (Gemini South) and 10.67 km (Cerro Armazones). These values extend from less than two to just over eight times the Fresnel scale ($\sqrt{\lambda D}/2 = 1.27$ km, where wavelength λ is 720 nm and D is the distance to Charon).

Models for straight-edge diffraction by a limb, integrated over the exposure interval for each frame, were fitted separately to the

points are plotted at the midpoint of each exposure, with respect to seconds after 03:35:00 UT. Geometric limb times from model fits to the light curves are **a**, immersion 73.744 ± 0.001 s, emersion 130.563 ± 0.002 s, **b**, immersion 73.792 ± 0.005 s, emersion 130.609 ± 0.004 s, **c**, immersion 75.50 ± 0.15 s, emersion 130.55 ± 0.15 s and **d**, immersion 76.99 ± 0.04 s, emersion 114.28 ± 0.03 s. Signal-to-noise ratios of the data, calculated from light-curve fit residuals and normalized to a 1 s cycle, are **a**, 273, **b**, 117, **c**, 108, and **d**, 28. The anomalously high points prior to immersion and post emersion in the Clay data result from the first diffraction fringe.

immersion and emersion portions of each light curve. Free parameters of the models included background, full scale, geometric limb occultation time, and effective wavelength. As the dominant averaging effect was integration time, the occulted star was assumed to be a point source, and effects due to transfer time and smearing over a large band of wavelengths were not included. The resulting geocentric limb occultation times at each site were used to calculate Charon's radius. We have assumed that Charon is spherical and reserve asymmetric shape analysis for future work.

We find that the mean radius of Charon is 606 ± 8 km. The formal radius error from the least-squares fit to a strict circular solution is much smaller (0.04 km) because of our excellent time resolution; however, we feel that this is an underestimate given the sparse sampling of the limb and a suggestion of non-circularity from the Gemini South chord length. Further details concerning our calculation of the radius and error bar are available in Supplementary Information. The radius we find is consistent with previous measurements⁵ and the lower limit established from the previous stellar occultation observation⁴. Assuming that Charon is spherical and has

Table 1 | Upper limits on atmosphere candidate gases

Gas	Molecular weight (a.m.u.)	Refractivity* (10^{-4})	Scale height† (km)	Number density upper limit‡ (10^{13} cm $^{-3}$)	Column height upper limit‡ (cm am)
CH ₄	16.04	4.37	90 \pm 13	2.0	7.8
H ₂ O	18.02	2.50	79 \pm 12	3.4	11.4
Ne	20.18	0.67	71 \pm 10	11.9	36.0
N ₂	28.01	2.95	51 \pm 8	2.3	5.0
CO	28.01	3.33	51 \pm 8	2.0	4.4
Ar	39.95	2.83	36 \pm 5	2.0	3.1
CO ₂	44.01	4.47	32 \pm 5	1.2	1.7
Kr	83.80	4.25	17 \pm 3	0.9	0.7
Xe	131.29	6.97	11 \pm 2	0.4	0.2

* At standard temperature and pressure, for wavelengths ranging from 6,438 to 7,056 Å (ref. 11).

† Assuming Charon is spherical, with radius 606 ± 8 km, mass $(1.60 \pm 0.12) \times 10^{24}$ g, and surface temperature 50 K.

‡ Upper limits are 3σ , for an isothermal atmosphere. The number density limit applies to surface density. The upper limits on column height are written in units of centimetre amagats (cm am).

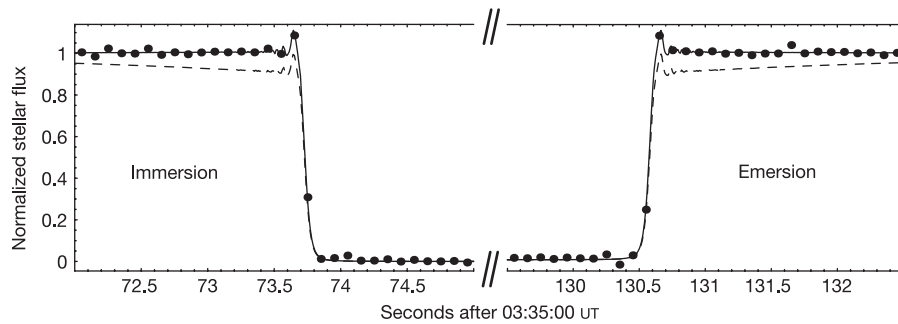


Figure 3 | Atmospheric model fits to the light-curve data. The segments of the Clay light curve shown here have been expanded such that individual data points are resolved, and the first diffraction fringe is clearly visible during immersion and emersion. A diffraction model with a tenuous atmosphere (solid line), from which our 3σ upper limit is derived, is displayed. To illustrate the effect of a substantial atmosphere, a second

model is also shown (dashed line), which represents a 50-km scale height and a 10% flux drop at the surface ($b = 0.10$). This model merges with the data baseline beyond the limits of the plot. The differential bending in the dashed-line model has been enhanced significantly with respect to our upper limit ($b = 0.015$).

a mass of $(1.60 \pm 0.12) \times 10^{24}$ g (ref. 2), we find its density to be 1.72 ± 0.15 g cm $^{-3}$. For ice density 1.0 g cm $^{-3}$ and rock density 3.0 g cm $^{-3}$, we derive a rock-mass fraction of 0.63 ± 0.05 . This value suggests that Charon contains a smaller fraction of rock by mass than Pluto (0.73 ± 0.06 ; refs 2, 5) and Neptune's moon Triton (0.77 ± 0.01 ; ref. 8).

We utilized the detection of the first diffraction fringe in the Clay data to perform model fitting for a thin, isothermal atmosphere in the presence of limb diffraction^{9,10}. Additional parameters for this model included atmospheric scale height and differential bending (H and b)⁹, in the regime where H is much greater than the Fresnel scale. For small flux drops, the differential bending parameter b equals the drop in normalized flux at the surface radius. We selected several likely atmospheric constituents⁴, listed in Table 1. The diffraction models were run over the range of scale heights appropriate for these candidates. Based on the lack of significant flux drop in the data (indicative of no significant atmosphere), we set a 3σ upper limit for differential bending of $b = 0.015$. Figure 3 shows the tenuous-atmosphere model from which this limit was derived (solid line), along with data from the Clay light curve to which it was fitted. The dashed-line model in Fig. 3 illustrates the effect of an atmosphere an order of magnitude denser than the upper limit of the fitted model. From our upper limit on b , we derive a 3σ upper limit on the refractivity for an atmosphere composed of each candidate gas⁴. Refractivities of the gases at standard temperature and pressure¹¹ were then used to calculate upper limits on number density and column height.

The 3σ upper limits on number density for each of the prospective atmospheric constituents are listed in Table 1. The corresponding column heights are roughly a factor of two lower than those established from the previously observed stellar occultation by Charon⁴. Such low densities are consistent with Charon's anticipated high atmospheric loss rate and lack of replenishment mechanism^{12,13}. In context, the upper limits found here are orders of magnitude less than the density of N₂ near the surface of Triton ($\sim 10^{15}$ cm $^{-3}$; ref. 14) and at a radial distance of 1,205 km (the 3- μ bar pressure level in 2002) on Pluto (2.2×10^{14} cm $^{-3}$; refs 14–16). More apt comparisons are the tenuous atmospheres of Io, which is primarily SO₂ and has a number density of a few times 10^{10} cm $^{-3}$ (ref. 17), and Mercury, with a total subsolar atmospheric density of $< 10^7$ cm $^{-3}$ (ref. 18). Leading candidate gases of which a tenuous atmosphere on Charon may be composed are H₂O, N₂, Ar (ref. 19) and CO (ref. 20). Spectroscopic observations of Charon's surface indicate the presence of H₂O ice^{21,22} mixed with a neutral absorber²³. Other studies have suggested that volatiles could be present on the surface²⁴, perhaps located in shadowed regions¹³. However, the low vapour pressure of H₂O renders it an unlikely atmospheric constituent⁴ and recent spectral

analyses find no indication of volatile ices such as CO, CH₄ or N₂ on Charon's surface²³. The absence of an obvious atmospheric candidate gas is consistent with the lack of a significant atmosphere in the occultation data.

The rock-mass fraction we find for Charon, in addition to those of Pluto and Triton, is higher than the maximum (~ 0.5) predicted by models of outer solar nebula condensates⁸. One explanation is a collisional origin for Pluto–Charon, during which there was a possibility for jetting of icy mantle material⁶. Charon's effective lack of atmosphere could also be explained by a volatile-removing collision⁶. The density we find for Charon is lower than the system mean, which seems consistent with an impact if either precursor object were differentiated⁶. In this case, an impactor could have collided with a differentiated proto-Pluto, leaving a disk of preferentially lower-density material that resulted in a satellite depleted in heavier elements (a situation that has a parallel in the Earth–Moon system)^{6,25}.

This successful observation of a stellar occultation by Charon is encouraging for establishing sizes and probing for atmospheres of large Kuiper belt objects, such as the newly discovered 2003 UB₃₁₃, 2005 FY₉ and 2003 EL₆₁ (ref. 26). In particular, 2003 UB₃₁₃ has approximately Charon's angular diameter and is a prime candidate for having a bound atmosphere, because methane has been detected on its surface²⁷ and it is larger than Pluto.

Received 2 August; accepted 21 September 2005.

1. Null, G. W. & Owen, W. M. J. Charon/Pluto mass ratio obtained with HST CCD observations in 1991 and 1993. *Astron. J.* **111**, 1368–1381 (1996).
2. Olkin, C. B., Wasserman, L. H. & Franz, O. G. The mass ratio of Charon to Pluto from Hubble Space Telescope astrometry with Fine Guidance Sensors. *Icarus* **164**, 254–259 (2003).
3. Walker, A. R. An occultation by Charon. *Mon. Not. R. Astron. Soc.* **192**, 47p–50p (1980).
4. Elliot, J. L. & Young, L. A. Limits on the radius and a possible atmosphere of Charon from its 1980 stellar occultation. *Icarus* **89**, 244–254 (1991).
5. Tholen, D. J. & Buie, M. W. in *Pluto and Charon* (eds Stern, S. A. & Tholen, D. J.) 193–219 (Univ. Arizona Press, Tucson, 1997).
6. McKinnon, W. B. On the origin of the Pluto–Charon binary. *Astrophys. J.* **344**, L41–L44 (1989).
7. McDonald, S. W. & Elliot, J. L. Pluto–Charon stellar occultation candidates: 2000–2009. *Astron. J.* **119**, 1999–2007 (2000); Erratum. **120**, 1599 (2000).
8. McKinnon, W. B., Simonelli, D. P. & Schubert, G. in *Pluto and Charon* (eds Stern, S. A. & Tholen, D. J.) 295–343 (Univ. Arizona Press, Tucson, 1997).
9. French, R. G. & Gierasch, P. J. Diffraction calculation of occultation light curves in the presence of an isothermal atmosphere. *Astron. J.* **81**, 445–451 (1976).
10. Bartholdi, P. & Owen, F. The occultation of Beta Scorpii by Jupiter and Io. II. *Icarus* **77**, 60–65 (1972).
11. National Research Council (U.S.). *International Critical Tables of Numerical Data, Physics, Chemistry, And Technology* (eds West, C. J. & Hull, C.) (McGraw-Hill Book Co., New York, 1933).

12. Trafton, L., Stern, S. A. & Gladstone, G. R. The Pluto-Charon system: The escape of Charon's primordial atmosphere. *Icarus* **74**, 108–120 (1988).
13. Yelle, R. V. & Elliot, J. L. in *Pluto and Charon* (eds Stern, S. A. & Tholen, D. J.) 347–390 (Univ. Arizona Press, Tucson, 1997).
14. Elliot, J. L., Person, M. J. & Qu, S. Analysis of stellar occultation data. II. Inversion, with application to Pluto and Triton. *Astron. J.* **126**, 1041–1079 (2003).
15. Elliot, J. L. *et al.* The recent expansion of Pluto's atmosphere. *Nature* **424**, 165–168 (2003).
16. Pasachoff, J. M. *et al.* The structure of Pluto's atmosphere from the 2002 August 21 stellar occultation. *Astron. J.* **129**, 1718–1723 (2005).
17. Spencer, J. *et al.* Mid-infrared detection of large longitudinal asymmetries in Io's SO₂ atmosphere. *Icarus* **176**, 283–304 (2005).
18. Broadfoot, A. L., Shemansky, D. E. & Kumar, S. Mariner 10: Mercury atmosphere. *Geophys. Res. Lett.* **3**, 577–580 (1976).
19. Stern, S. A. & Trafton, L. Constraints on bulk composition, seasonal variation, and global dynamics of Pluto's atmosphere. *Icarus* **57**, 231–240 (1984).
20. Yelle, R. V. & Lunine, J. I. Evidence for a molecule heavier than methane in the atmosphere of Pluto. *Nature* **339**, 288–290 (1989).
21. Marcialis, R. L., Rieke, G. H. & Lebofsky, L. A. The surface composition of Charon: Tentative identification of water ice. *Science* **237**, 1349–1351 (1987).
22. Buie, M. W., Cruikshank, D. P., Lebofsky, L. A. & Tedesco, E. F. Water frost on Charon. *Nature* **329**, 522–523 (1987).
23. Buie, M. & Grundy, W. M. The distribution and physical state of H₂O on Charon. *Icarus* **148**, 324–339 (2000).
24. Roush, T. L. Charon: more than water ice? *Icarus* **108**, 243–254 (1994).
25. Canup, R. M. A giant impact origin of Pluto-Charon. *Science* **307**, 546–550 (2005).
26. Brown, M. E., Trujillo, C. A. & Rabinowitz, D. L. 2003 EL_61, 2003 UB_313, and 2005 FY_9. *IAU Circ.* **8577** (2005).
27. Trujillo, C. A., Barkume, K. M., Brown, M. E., Schaller, E. L. & Rabinowitz, D. L. Near infrared spectra from Mauna Kea of the new brightest Kuiper Belt Object. *Bull. Am. Astron. Soc.* **37**, 52.06 (2005).
28. USNO. *The Astronomical Almanac for the Year 2005* (US Govt Printing Office, Washington DC, 2003).

Supplementary Information is linked to the online version of the paper at www.nature.com/nature.

Acknowledgements B.A.B., J.W.G. and T.T. are Guest Observers at Instituto de Astronomía, Universidad Católica del Norte, Antofagasta, Chile. We thank N. Vogt and M. Murphy of Universidad Católica del Norte for their expertise, assistance, and the use of their telescope at Cerro Armazones; G. Gutiérrez and F. Sánchez, telescope operators at Las Campanas; R. Carrasco, K. Volk (observers), and E. Wendroth (telescope operator) at Gemini South; M. Ottoboni and R. Campos at Pico Dos Dias; and C. Czelusniak, assistant observer from Universidade Estadual de Ponta Grossa. Full credits for Gemini Observatory are available at <http://www.us-gemini.noao.edu/sciops/data/dataAcknowIndex.html>. Support for this work was provided by NASA Planetary Astronomy. Additional support was provided by the Belgian Federal Office for Scientific, Technical and Cultural Affairs and the Flemish Ministry for Foreign Policy, European Affairs, Science and Technology.

Author Information Reprints and permissions information is available at npg.nature.com/reprintsandpermissions. The authors declare no competing financial interests. Correspondence and requests for materials should be addressed to A.A.S.G. (gulbis@mit.edu).

Supplementary Discussion: Adopted Radius and Error Bar

We determined our mean radius and error using a set of four different least-squares fits to the geometric limb occultation times for the four chords shown as light curves in Fig. 2. The first fit was for a circular figure, with each geometric limb point weighted inversely as the square of its timing error. The second fit was also for a circular figure, but unweighted. The third and fourth fits were weighted and unweighted fits for an elliptical figure. We chose an ellipse not because we think Charon's figure is an ellipse, but because it is a convenient analytic form for a first-order deviation from a circle.

The results of these fits were: (i) the mean radii for the weighted and unweighted versions of the circular fit agree reasonably well with each other, (ii) the mean radii for the weighted and unweighted versions of the elliptical fit agree reasonably well with each other, (iii) there is a large difference between the mean radii for the circular fits and the mean radii for the elliptical fits, and (iv) the fitted ellipticity is not statistically significant (hence we choose not to report it).

If Charon's figure were circular and there were no systematic errors in any of the geometric limb times, then the results of the first fit (606.015 +/- 0.039 km) would be valid. While at first glance this error may seem exceptionally small, it is due to the domination of the fit by the chords with the most accurate timing. In this case, two points of the circle were firmly anchored by the Clay and du Pont times. Since this chord happens to be very close to the centerline, the formal error in the radius is controlled by the accuracy of this chord more than by the Cerro Armazones and Gemini South chords. Errors in these outlying chords allow the circle to move up and down, which causes only a small perturbation in the length of the (nearly) centerline chord set by the Clay and du Pont data.

The residuals from the weighted, circular fit for all stations except for Gemini South were reasonably consistent with their timing errors. One explanation for the Gemini South residuals might be a timing issue, since the timing at Gemini South was set by Network Time Protocol (NTP) and not a GPS (as was used to time the other three light curves). We do not think that the difference between NTP and GPS time could be large enough to explain the residuals, so we sought an explanation for the residuals by invoking a non-circular figure of Charon. This could be due either to a Charon being a smooth, non-circular figure or to local topography. From our dataset alone, we cannot distinguish between these two explanations.

Whatever the reason for the deviation from a circular figure, we chose to estimate the uncertainty in the mean radius of Charon by the difference between the mean radius for the circular weighted fit (606 km) and the mean radius for the elliptical weighted fit (598 km). This results in an 8-km error bar.

Table S1. Observation details

Site,* aperture, telescope	West longitude† (° ' ")	Latitude† (° ' ")	Altitude (km)†	Field of view (square arcsec)	Plate scale (arcsec/ binned pix)‡	Data rate§ (Hz)	Occultation times (s after 03:35:00 UT)		SNR¶	Observers
							Immersion	Emersion		
Pico dos Dias 0.6-m Zeiss Cerro Armazones	45 35 00	-22 32 07	1878	225	0.88 (2)	2	#	#	#	jmp, sps, me
0.84-m	70 11 46	-24 35 52	2763	419.8	1.64 (2)	2	76.99±0.04	114.28±0.03	28	bab, mjp, jwg, tt
Las Campanas 2.5-m du Pont	70 42 13	-29 00 26	2327	88.6	1.04 (6)	5	73.792±0.005	130.609±0.004	117	aasg, djo
6.5-m Clay Cerro Pachón☆	70 41 33	-29 00 51	2429	23.5	0.18 (4)	10	73.744±0.001	130.563±0.002	273	jle, era
8-m Gemini S.	70 43 24	-30 13 42	2725	30.7**	0.24 (2)	~2.24	75.50±0.15	130.55±0.15	108	sdk

* Observatory key: Pico dos Dias – Laboratório Nacional de Astrofísica's Observatório Pico dos Dias, Itajubá, Brazil; Cerro Armazones – Observatório Cerro Armazones, Antofagasta, Chile; Las Campanas – Las Campanas Observatory, La Serena, Chile; Cerro Pachón – Gemini South, La Serena, Chile.

† Coordinates were obtained from POETS GPS surveys at Pico dos Dias, Cerro Armazones and Las Campanas, and the Astronomical Almanac²⁸ for Gemini South.

‡ Number of binned pixels is in parentheses. All binning is square.

§ Integration times are 1.74 ms less than the data rate for all sites excluding Gemini South, where the integration time was 0.30 s and the remaining 0.146 ± 0.001 s of the cadence was required for readout.

|| Geometric limb times, from model fits to the light curves. Since the cadence at Gemini South was not fast enough to sample the diffraction pattern, its timing errors are estimated to be equal to the deadtime.

¶ Signal-to-noise ratios are calculated from light-curve fit residuals and normalized to a 1-s cycle.

Observations were unsuccessful due to clouds.

☆ Observations on this telescope were taken using the Acquisition Camera (a 1024×1024 EEV CCD47 with 13-micron pixels) and the R_G0154 filter (610-750 nm). Data at all other sites were obtained with Portable Occultation, Eclipse, and Transit Systems (POETS) and no filter. POETS cameras utilize back-illuminated CCDs (E2V CCD97), 512×512 arrays of 16 micron pixels, with $> 90\%$ quantum efficiency. POETS CCDs were thermoelectrically cooled between -50° and -70° C to effectively eliminate dark current, and the read noise was ~ 6 electrons rms.

** Full field of view of the instrument. A 128×128 pixel subframe (15.4 square arcsec) was recorded for these observations.